

1 **S1. Supplement**

2 **S1.1. Circular polarisation in transmission and reflection**

3 The polarisation component perpendicular to the main pulse ( $E_2$ , linearly-polarized and parallel  
 4 to x-axis, p-pol.) should originate from the region of THz wave emission and to contribute to the  
 5 formation of circular-polarized THz wave emission similarly to the action of a birefringence  $\lambda/4$   
 6 waveplate which combines two x- and y-pol. with phase separation of  $\pi/2$  for the conversion  
 7 from linear to circular polarisation. For long self-guided cm-long filaments in air, polarisation  
 8 is linear-radial due to on-axis charge separation as result of ponderomotive action [1]. At an  
 9 approximately twice longer delay time of 9.7 ns, the polarisation of THz wave emission becomes  
 10 left-handed circular, while at the most intense case at 4.7 ns it was right-handed circular. It is  
 11 consistent with an accumulated phase  $\Delta\psi$  between two x- and y-polarised harmonics following the  
 12 equation of ellipsis  $(E_y/E_{oy})^2 + (E_x/E_{ox})^2 - 2(E_x/E_{ox})(E_y/E_{oy}) \cos \Delta\psi = \sin^2 \Delta\psi$ , where  
 13  $E_{ox,oy}$  are the amplitudes of the corresponding fields and  $\Delta\psi$  is the phase added to the  $E_y$ -field.  
 14 Circularly (elliptically when  $E_{ox} \neq E_{oy}$ ) -polarised light results when  $\Delta\psi = \pm\pi/2$  while for the  
 15  $\Delta\psi = \pm\pi/4$  the axes of the polarisation ellipsis are inclined by  $\pi/4$  in respect to the xy-frame.  
 16 Figure S1 shows the results which are consistent with this polarisation formation where  $\Delta t \propto \Delta\psi$   
 17 and the THz wave emission in the reflection direction experiences a smaller phase delay due to  
 18 not traversing the water flow as compared with the case in the transmission direction. Hence, a

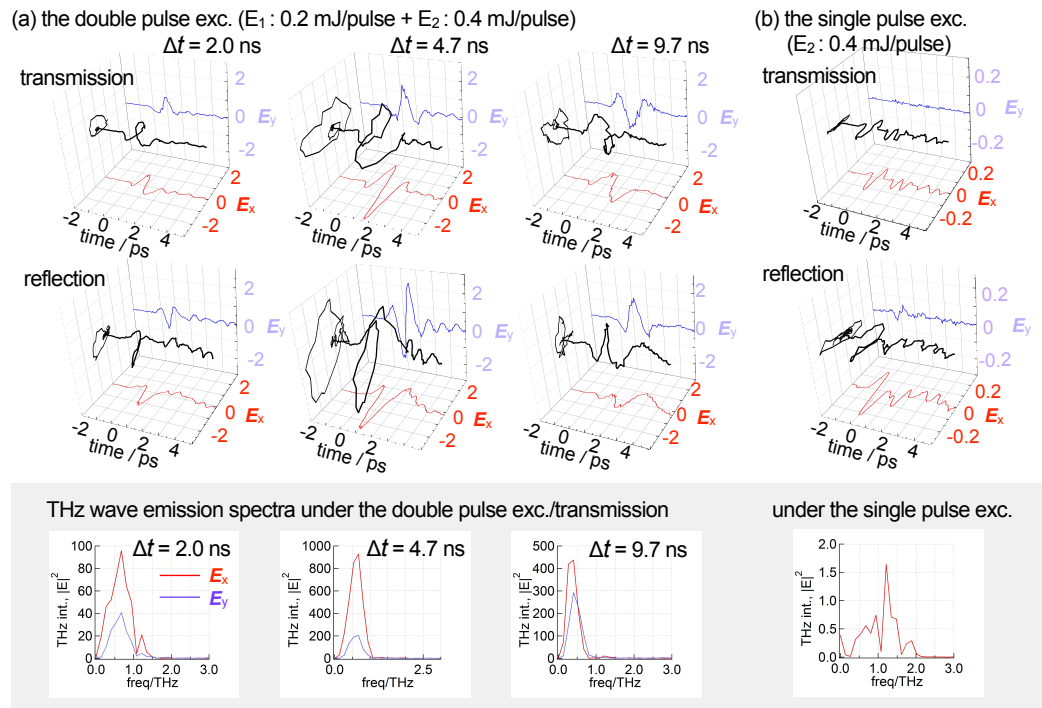


Fig. S1. Signals in THz time-domain spectroscopy and polarization status of THz electric-fields under (a) the double pulse excitation with the pre-pulse ( $E_1$ , y-pol., 0.2 mJ/pulse) in the transmission and the reflection directions in different delay times,  $\Delta t$  and (b) the single pulse excitation (only with the main pulse,  $E_2$ , x-pol., 0.4 mJ/pulse). The inset with gray-colored background at the bottom represents THz wave emission spectra obtained in discrete Fourier-transform of TDS signals in the transmission direction.

19  $\pi/4$  inclined ellipsis is obtained in the reflection direction.

20 In the reflection direction, THz wave emission has the same one-cycle rotation electric field but  
 21 with opposite left-handed circularly-polarization as shown in Fig. S1. This is due to the reflection  
 22 of THz wave from the water flow at the angle of laser incidence  $60^\circ$  which cause a 0 phase flip  
 23 for the p-pol. (x-pol.) while  $\pi$  for s-pol. (y-pol.) as mandated by the Fresnel reflection rules.  
 24 This changes the handedness of THz wave emission in the reflection direction, however, does  
 25 not decrease its intensity due to absorption in water as for the transmission direction. By fine  
 26 TDS measurements shown in Fig. 1(d), it was also confirmed that the reflected THz wave arrives  
 27 faster than the transmitted one which is due to absence of water film in the reflection geometry.

## 28 S1.2. Shockwave dynamics

29 Refractive indexes of air at pressures up to 5 atmospheres have been directly measured from THz  
 30 time-domain spectroscopy in the wide spectral range [2]. The refractive index,  $n$ , was found  
 31 closely following the Hauf–Grigull law dependence on density  $\rho$ :  $n(\rho) - 1 = \frac{3}{2} \frac{rMP}{RT}$ , where  $r$  is  
 32 the refractivity of gas,  $M$  its molar mass,  $P$  is the pressure,  $R$  is the ideal gas constant, and  $T$   
 33 is the absolute temperature of gas. At constant temperature (e.g., across the shock front), the  
 34 refractive index depends on the gas pressure and molar refractivity  $R_n = \frac{M}{\rho} \frac{n^2-1}{n^2+2}$ , which defines  
 35 the polarizability  $\alpha' = 3R_n/(4\pi N_A)$ ; here  $N_A$  is the Avogadro number. The refractive index was  
 36 found following the linear dependence vs. pressure as determined from direct measurements  
 37 for the tested gases; for  $N_2$  (air)  $n = 1 + 2.39 \times 10^{-3} P$  [2]. For sake of estimate at a very high  
 38 pressures of  $\sim 500$  atm encountered at the shockwave front of a strong explosion, the refractive  
 39 index would reach  $n \approx 2.2$ , which is similar to that of water at the explored THz spectral range  
 40 1-3 THz of this study.

41 Figure S3 shows the temporal evolution of the shockwave front recognizable in shadowgraphs  
 42 captured by white light continuum back-illumination. A dynamic explosion triggered by the  
 43 pre-pulse is clearly visualised. The radius  $R$  of the shockwave is increasing in time  $t$  as [3]:

$$R(t) = \left( \frac{E_p}{K(\gamma)\rho_0} \right)^{1/(2+i)} t^{2/(2+i)}, \quad (S1)$$

44 where  $E_p$  is the instantaneous (in space and time) release of energy,  $K(\gamma) = (0.6 - 0.8)$  is the  
 45 constant dependent on the adiabatic coefficient  $\gamma = C_p/C_v$  ( $\gamma = 1.4$  for air),  $\rho_0$  is the mass  
 46 density on unperturbed medium, and  $i$  is the dimensionality coefficient  $i = 3$  for spherical and  
 47  $i = 2$  for cylindrical explosion; here  $C_{p,v}$  are the heat capacities at constant pressure and volume,  
 48 respectively. Figure S3 shows that the cylindrical explosion is the better fit for the shadowgraphs  
 49 shown in Fig. S2. The diameters plotted in Fig. S3 correspond to the circle which best fit the  
 50 transverse cross section of the shocked region.

51 The maximum volume occupied by a shock wave in a surrounding of atmospheric air (pressure  
 52  $\rho_0 = 101325 \approx 10^5$  Pa) can be estimated from the absorbed pulse energy  $E_p$  divided by the  
 53 spherical shocked volume with radius  $r_{sh} = \sqrt[3]{\frac{3E_p}{4\pi\rho_0}}$ , which is  $r_{sh} = 980 \mu\text{m}$  for  $E_2 = 0.4$  mJ  
 54 (a fully absorbed energy of the second pulse). At this distance, shock wave becomes a usual  
 55 pressure wave and travels at the speed of sound at normal conditions. A spherical surface is  
 56 acting as a lens of the focal length equal to the half of the curvature  $F = r/2$  where  $r$  is the radius  
 57 and contributes to collimation of THz wave emitted as optical pulse travels through the ablated  
 58 water plume created by the pre-pulse  $E_1$ . Focusing by a spherical surface is shown in Fig. 2. Due  
 59 to a strong spherical aberration, the parallel rays are focused onto optical axis at distances slightly  
 60 larger than the  $F$  (out of water surface) as schematically shown in Fig. 2.

61 It is instructive to estimate a density jump across the shock front [3]:

$$\frac{\rho}{\rho_0} = \frac{(\gamma + 1)M^2}{(\gamma - 1)M^2 + 2}, \quad (S2)$$

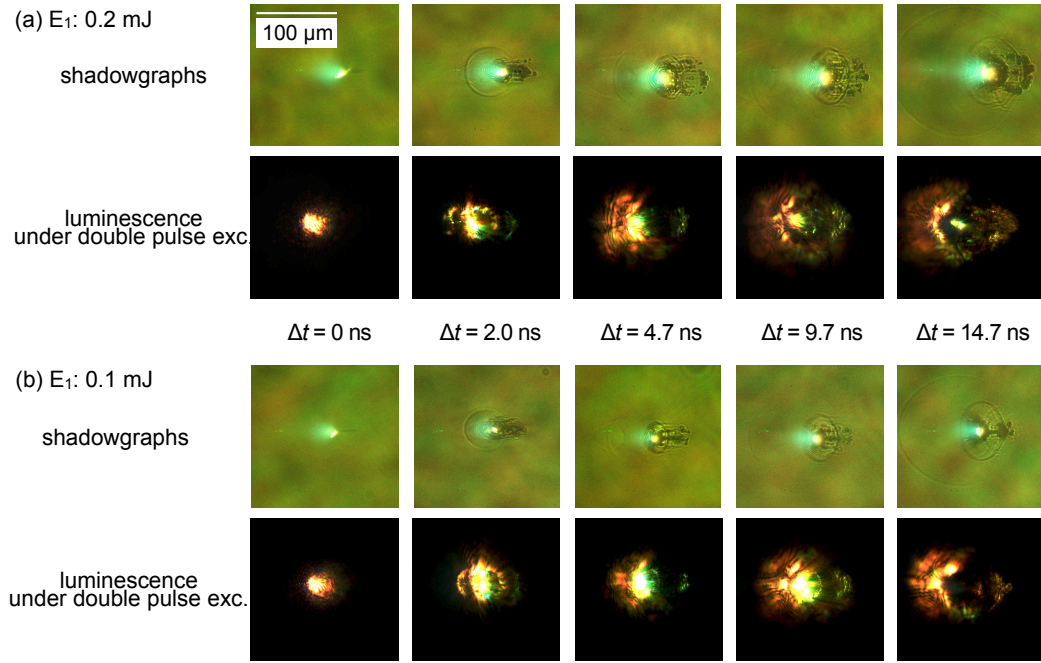


Fig. S2. Shadowgraphs under the pre-pulse irradiation with back-illumination of white light continuum ( $580 \pm 30$  nm) as a picosecond strobe light and luminescence images under the double pulse excitations with different pre-pulse intensities at (a) 0.2 mJ and (b) 0.1 mJ. The times indicated represent the delay time,  $\Delta t$ , after the pre-pulse irradiation. The images are on  $y$ - $z$  plane and the incident excitation pulses irradiate from the left side. The white spots in shadowgraphs are due to plasma emission induced by the pre-pulse irradiation.

62 where  $M = v_{sh}/v_s$  is the Mach number defined by ratio of  $v_{sh}$  shock and  $v_s$  sound velocities  
63 ( $v_s = 0.343$  km/s in air at normal conditions). The shockwave with speed  $v_{sh} = 7.6$  km/s was  
64 generated at the used two pulse  $E_1 + E_2 = (0.2+0.4)$  mJ irradiation conditions which corresponds  
65 to strong explosion with Mach number  $M = 22.2$ . The density increase of  $\rho/\rho_0 = 5.9$  (Eqn. S2)  
66 occurs across the shock front.

67 The pressure change at the shock front is [3]:

$$\frac{P}{P_0} = \frac{2\gamma M^2 - (\gamma - 1)}{\gamma + 1}. \quad (\text{S3})$$

68 For the  $M = 22.2$ , the pressure increase reaches  $\frac{P}{P_0} = 572.6$ . With these estimates for pressure  
69 and density increase, one would expect high refractive index changes approaching  $n > 2.2$  at the  
70 THz spectral band as discussed above.

71 It is clearly discernible that shockwave was also excited inside the water flow (Fig. S3). It was  
72 better visualised when pre-pulse was  $E_1 = 0.1$  mJ since a single linear modification inside water  
73 was observed rather multi-filaments observed at larger pulse energies. The shocked region inside  
74 water expanded over a cylinder of  $35 \mu\text{m}$  radius during 15 ns ( $v_{sh} = 2.3$  km/s) corresponding to  
75  $M = 1.6$  for sound speed in water  $v_s = 1.48$  km/s. When  $M < 2$ , explosion is not considered  
76 strong. The most prominent feature of water-jet irradiation with a pair of sub-mJ-pulses was a  
77 strong shock wave launched into surrounding air in front of the jet.

78 Evolution of micro-explosion is characterized by the independent parameters: energy  $E$  (or

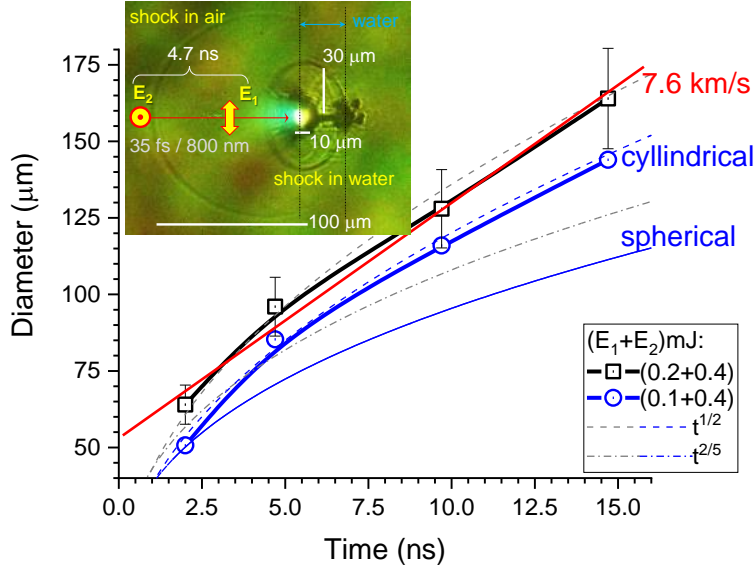


Fig. S3. Diameter of the shockwave at different delay time,  $\Delta t$ , after the pre-pulse irradiation ( $E_1$ ). The inset shows the shadowgraph at the delay time 14.7 ns when the pre-pulse intensity is 0.1 mJ. The back-light through a 17- $\mu\text{m}$ -thick water flow was the white light continuum converted from the main pulse  $E_2$ . The apparent thickness of the 17- $\mu\text{m}$  water flow is 34  $\mu\text{m}$  in the front view due to the 60° angle of incidence onto the water flow. Time scaling for temporal evolution of the shock radius in the case of spherical ( $i = 3$ ) and cylindrical ( $i = 2$ ) explosion is shown by  $R \propto t^{2/(i+2)}$  lines (see Eqn. S1). Slope of 7.8  $\mu\text{m}/\text{ns}$  is shown as an eye guide; error bars are 10%.

79 pressure  $P$ ), density  $\rho$ , and radius  $r$ , while the two other parameters required for the full description  
80 of the hydrodynamic processes the velocity and time can be expressed as  $v = \sqrt{P/\rho} \equiv \sqrt{E/(r^3\rho)}$   
81 and  $t = r^{5/2}\sqrt{\rho/E}$ , respectively. We showed that micro-explosions triggered by tightly focused  
82 fs-laser pulses are self-similar with macro-explosions made by a  $10^{21}$  large energy deposition  
83 when the time  $t$  and space  $r$  are  $10^7$  times larger [4]. All hydro-dynamic phenomena with the  
84 same initial pressure and density but differing in space and time scales are described by the same  
85 hydrodynamic equations.

### 86 S1.3. Estimates of light-matter interaction

87 Estimates of light-matter interaction and polarisation of THz wave emission under the experimental  
88 conditions are presented next.

89 **Water conversion to plasma by the pre-pulse irradiation.** Laser focusing for the laser  
90 pulse ( $\lambda = 800$  nm,  $t_p = 35$  fs) was carried out with an off-axis parabolic mirror with effective  
91 numerical aperture  $NA = 0.125$ . The focal spot area was  $S_f = 4.3 \times 10^{-7}$   $\text{cm}^2$  for the focal  
92 diameter  $1.22\lambda/NA \approx 7.4$   $\mu\text{m}$ . The energy of the pre-pulse ( $E_1$ ) and the main-pulse ( $E_2$ ) was  
93  $(1 - 4) \times 10^{-4}$  J. The corresponding pulse fluence was  $F = 230 - 920$   $\text{J}/\text{cm}^2$ , which is hundreds  
94 times higher than the ablation threshold of wide-bandgap ( $E_g > 6$  eV) materials  $\sim 2$   $\text{J}/\text{cm}^2$  [5, 6].  
95 At this intensity range of  $6.57 \times 10^{15} - 2.63 \times 10^{16}$   $\text{W}/\text{cm}^2$  (the pre- and main-pulses), both pulses  
96 ionise in the tunnelling regime and, most probably, more than two electrons are stripped off from  
97 oxygen. Visualisation of air breakdown under the experimental conditions had an axial extension  
98  $\sim 120 - 150$   $\mu\text{m}$ , which is close to the depth-of-focus which is  $2z_R$  where the Rayleigh length  
99  $z_R = \pi n w_0^2/\lambda \approx 60$   $\mu\text{m}$  with  $w_0 = 0.61\lambda/NA$  being the waist of the beam for the numerical

100 aperture  $NA = 0.125$  focusing.

101 Heat conductivity of water is  $0.6085 \text{ W/m.K}$ , heat capacity  $C_w = 75.35 \text{ J/(mol.K)}$  or  
102  $4.186 \text{ J/(g.K)}$ , heat of vaporisation  $Q_{ev} = 2.257 \text{ kJ/g}$ , the binding energy  $\epsilon_b = 4.2 \text{ eV/molecule}$   
103 or  $1.4 \text{ eV/atom}$ . The molecular number density  $n_a = \rho N_a / M_w = 3.35 \times 10^{22} \text{ molecules/cm}^3$ ,  
104 where  $\rho = 1 \text{ g/cm}^3$  is mass density of water,  $M_w = 18 \text{ g/mol}$  its molar mass, the dipole moment  
105  $1.846 \text{ D}$  (Debye  $D = 1 \times 10^{-18} \text{ statcoulomb.cm}$ ). The minimum energy required to ablate  
106  $m = 1 \text{ g}$  of water is  $Q_{ab} = m(C_w \Delta T + Q_{ev}) = 2.57 \text{ kJ}$  (corresponds to removal of material in a  
107 thermodynamic equilibrium). The pre-pulse at  $0.1 \text{ mJ}$  can evaporate  $3.89 \times 10^{-8} \text{ g}$  (or  $\text{cm}^3$ ) of  
108 water.

109 If the whole energy of the pre-pulse ( $10^{-4} \text{ J}$ ;  $I = 6.57 \times 10^{15} \text{ W/cm}^2$ ) is spent on ablation,  
110 the number of molecules in ablation is estimated to be  $N_{ab} = E_l / \epsilon_b = 10^{-4} / (4.2 \times e) =$   
111  $0.149 \times 10^{15}$  molecules or  $0.44 \times 10^{-9} \text{ cm}^3$  volume, where  $e$  is the electron charge. Therefore,  
112 the pre-pulse with  $10^{-4} \text{ J}$  irradiating the flow surface of  $S_f = 4.3 \times 10^{-7} \text{ cm}^2$  can ablate the  
113 volume in  $0.44 \times 10^{-9} [\text{cm}^3] / 4.3 \times 10^{-7} [\text{cm}^2] \approx 10 \mu\text{m}$  depth at maximum (taking into account  
114 ionization losses and heating it would be less as it is shown later).

115 Absorbed energy density is defined as the following:  $\epsilon_{abs} [\text{J/cm}^3] = A \times F / l_{abs}$ . Assuming that  
116 at least 2-3 electrons are stripped off from oxygen and 2 electrons from hydrogen, the electron  
117 number density is around  $10^{23} \text{ cm}^{-3}$ . Then, the plasma frequency  $\omega_{pe} \approx 10^{16} \text{ s}^{-1} \approx \nu_{eff}$  is an  
118 effective collision rate Using the dielectric function in the Drude approximation for plasma, one  
119 gets  $\epsilon_{re} \approx 0$  or  $n = k$  (the real and imaginary parts of the refractive index);  $\epsilon_{im} \approx \nu_{eff} / \omega = 2n^2$   
120 and  $n = 1.457$  [7]. Then, the Fresnel absorption coefficient  $A = 4n / [(n+1)^2 + n^2] = 0.714$  and  
121 the absorption length  $l_{abs} = 87 \text{ nm}$  defining the absorbed energy density  $\epsilon_{abs} = 18.9 \text{ MJ/cm}^3$   
122 and the maximum electron temperature (treating electrons as the ideal gas)  $T_{e,max} = 0.9 \times 10^7 \text{ K}$   
123 or  $0.79 \text{ keV}$ . This explains the origin of X-ray emission which is directly related to the plasma  
124 temperature.

125 **Electron-ion energy equilibration; huge space separation of protons and oxygen ions.**

126 The protons equilibrate the temperature with electrons in less than one picosecond while oxygen  
127 ions equilibrate in 16 times longer. After the electron-ion temperature equilibration (3 ions are  
128 added to every 5 electrons), the average temperature is  $0.5 \text{ keV}$ . The protons have 4 times higher  
129 velocity than oxygen ions,  $v_p = 3 \times 10^7 \text{ cm/s}$ ,  $v_O = 0.75 \times 10^7 \text{ cm/s}$  to the end of the pulse.  
130 Thus, after  $16 \text{ ps}$  protons are at  $4.8 \mu\text{m}$  ahead of oxygen ions.

131 The electrons are hot right after the beginning of the incident laser pulse. Therefore, during  
132 the laser pulse, electrons expand in the direction opposite to the incident laser pulse and pulling  
133 protons with them by the force of the electrostatic attraction (the Coulomb force). At the same  
134 time, a heat wave by electronic heat conduction moves inside the water flow with heating ions,  
135 ablate and expand them in the direction opposite to the laser pulse with velocity exceeding the  
136 sound velocity, approximately being around  $10^6 \text{ cm/s}$ . Then, heat wave converts to the shockwave  
137 when the heat wave velocity equals to the local sound velocity (electron-ion equilibration).  
138 Plasma cloud (current) has a complicated structure: long rarefied head of electrons and protons  
139 followed more dense mixture with oxygen ions and finally the densest part. By estimation, around  
140  $1.5 - 2 \mu\text{m}$  depth is ablated, much less than the maximum estimate above, because the plasma is  
141 very hot. After  $5 \text{ ns}$ , the major part of the ablated water expands approximately on  $50 \mu\text{m}$ . This  
142 scenario outlined from the deposited energy arguments alone is consistent with the shadowgraphy  
143 shown in Fig. S2.

#### 144 S1.4. Polarisation-related effects

145 **Radiation emission at the long distances from the time-dependent current.** In the considered  
146 case, the charges are first accelerating (second time derivative is positive) and afterwards are  
147 decelerating in the field of linearly-polarised laser pulse. Vector along the current is  $\mathbf{r}$ , direction  
148 to the detector located at the distance  $R_0$ , is  $\mathbf{n}$ . The size of the emitter,  $r$ , is much smaller than the

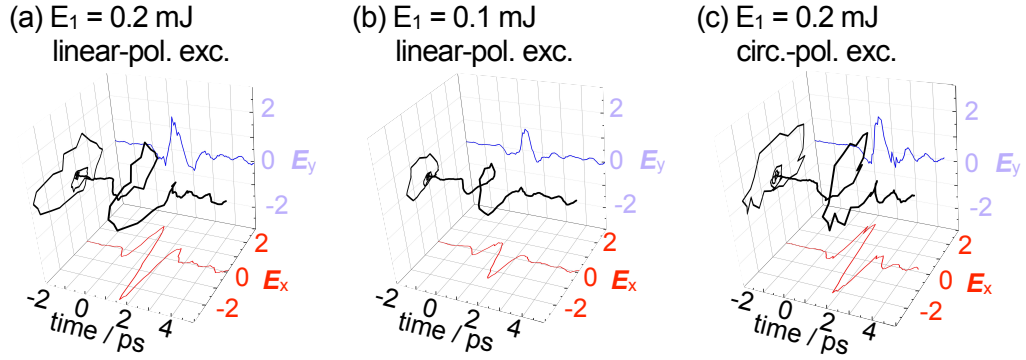


Fig. S4. Signals in time-domain spectroscopy (TDS) and polarization status of THz electric fields in the transmission direction for the pre-pulse ( $E_1$ ) intensity at (a) 0.2 mJ/pulse (reproduced from Fig. 2(a)) and (b) 0.1 mJ/pulse at the delay time of 4.7 ns. The main pulse ( $E_2$ ) intensity is fixed at 0.4 mJ/pulse. (c) The THz  $E$ -field transients when the pre- ( $E_1$ , 0.2 mJ) and the main ( $E_2$ , 0.4 mJ) pulses are contra-circularly-polarized (a  $\lambda/4$  waveplate for 800 nm was inserted in the optical path).

149 distance to observation,  $r \ll R_0$ . The emitted wave arrives at the detector as a plane wave. The  
 150 vector potential of the emitting field reads [8]:

$$\mathbf{A} = \frac{1}{cR_0} \int \mathbf{j} \times dV, \quad (\text{S4})$$

151 where  $c$  is the speed of light. The polarisation of the emitting field depends on the mutual  
 152 directions of the current and the direction to the observation point:

$$\mathbf{H} = \left( \frac{d\mathbf{A}}{dt} \times \mathbf{n} \right) / c, \quad \mathbf{E} = \left[ \left( \frac{d\mathbf{A}}{dt} \times \mathbf{n} \right) \times \mathbf{n} \right] / c. \quad (\text{S5})$$

153 Time dependence of the current defines the spectrum of the emitting radiation:  $\mathbf{j}_\omega = \int \mathbf{j}(t) \exp(i\omega t) dt$ .  
 154 For a linearly-oriented current transient, the emitting dipole field follows the  $\sin^2 \theta$  angular  
 155 dependence, where  $\theta$  is the polar angle. The second/main pulse irradiates the volume of  
 156 expanding water-air cloud ablated by the first  $E_1$  pulse and generates a 1-2 ps current transient  
 157 which emits circularly-polarised THz wave (Fig. S4). The origin of the current transients is the  
 158 charge displacement along polarisation of the traveling  $E$ -field of the fs-laser pulse  $E_2$  due to  
 159 ponderomotive force  $F_p \propto \nabla E_2^2$ . This force is radial (Gaussian-like intensity envelope of laser  
 160 pulse) and the diffusion of charges depleted on the optical axis caused currents with picosecond  
 161 duration. This charge density restoration and recombination current traveled along laser pulse in  
 162 the focal region which is approximately the Rayleigh length  $z_R \approx 60 \mu\text{m}$ , which is  $\lambda_{THz}/4$  for the  
 163 1.25 THz ( $240 \mu\text{m}$ ) emission. This axially traveling current with length of tens-of-micrometers  
 164 cause the circularly polarised THz emission. This explanation was further corroborated by  
 165 carrying the same experiment only with pre- and main-pulses at contra-circular polarisations.  
 166 This was achieved by inserting  $\lambda_{800nm}/4$  waveplate into the optical path. Figure S4(c) shows  
 167 the temporal evolution of  $E_{x,y}$  fields which is almost identical to the contra-linear polarised  
 168 experiment (a,b). It is consistent with ponderomotive charge displacement and relaxation scenario.  
 169 This explanation is based on THz emission located in front of the water flow as confirmed in a  
 170 separate experiment (as shown in Fig. 1(d)).

171 The difference of charge wave formation of self-guided filament at loose focusing (1D dynamics)  
 172 and at tight focusing and high intensity (2D and 3D dynamics) is very different. For the 1D wave

173 in plasma, the resonance conditions when amplitude is growing are at  $t_p \approx 1/\omega_p$  [9], where  $\omega_p$   
174 is plasma cyclic frequency. Plasma frequency  $\omega_p = 5 \times 10^4 \sqrt{n_e} \text{ s}^{-1}$  for the resonance is when  
175  $n_e = 4 \times 10^{14} t_{ps}^{-2} \text{ cm}^{-3}$ , where the laser pulse duration is in picoseconds  $t_{ps} = t_p/1$  [ps]. Hence  
176 for  $t_p = 100$  fs, the resonance is achieved when plasma density is  $n_e \approx 4 \times 10^{16} \text{ cm}^{-3}$  as it is  
177 typical for cm-long filaments in air [1]. For the short  $t_p = 35$  fs pulses used in this study, the  
178 resonance is at  $n_e \approx 3.27 \times 10^{17} \text{ cm}^{-3}$  which is above the molecular number density of air. The  
179 first pulse ablated water was contributing for larger amount of material and plasma density in the  
180 second pulse, which is at resonance for plasma wave when pulses are shorter. For stronger light  
181 intensity (tight focusing), the electrons are subjected to the magnetic part of the Lorenz force  
182  $\mathbf{F}_l = e(\mathbf{E} + \mathbf{v} \times \mathbf{B})$ . This cause electron oscillating not purely perpendicular to the wave vector  $\mathbf{k}$   
183 along  $\mathbf{E}$  with  $v = \frac{eE}{m_e \omega} \cos(\omega t)$ , but making a letter-8 trajectory in the  $(k, E)$ -plane [10, 11]. This  
184 is caused by the Lorenz force part of  $(\mathbf{v} \times \mathbf{B})$  becomes important as intensity is increasing towards  
185 the relativistic conditions when the electron quiver velocity is approaching  $a_0 = \frac{eE}{m_e \omega c} \sim 1$   
186 ( $a_0 = 0.85 \sqrt{I_{18} \lambda_\mu^2}$  where light intensity is normalised  $I_{18} = I/10^{18} [\text{Wcm}^{-2}]$  and  $\lambda_\mu = \lambda/1$  [ $\mu\text{m}$ ]).  
187 In our experiments we approach  $a_0 \approx 0.143$  at maximum  $E_2 = 0.4$  mJ pulse. How fast plasma  
188 responds to a perturbation can be estimated as a ratio of the Debye length  $\lambda_D = \sqrt{\frac{\epsilon_0 k_B T_e}{e^2 n_e}}$  and  
189 thermal velocity of electrons  $v_e = k_B T_e / m_e$ , where  $\epsilon_0$  is the permittivity of vacuum,  $k_B$  is the  
190 Boltzmann constant,  $e$ ,  $m_e$  are electron charge and mass, respectively. It is informative to evaluate  
191 the response time  $t_D = \lambda_D / v_e$  for the experimental conditions with  $n_e = 3 \times 10^{17} \text{ cm}^{-3}$  and  
192  $T_e = 10^7$  K:  $t_D = 32$  fs and  $\lambda_D = 398$  nm. The Debye sphere has a larger number of electrons  
193  $n_e \times \frac{4}{3} \pi \lambda_D^3 = 8 \times 10^4 \gg 1$ , hence the ideal plasma conditions.

194 A complex 3D dynamics of electron and ion currents inside the strongly non-homogeneous  
195 expanding plasma is reflected in the polarisation of THz wave emission as well as on its  
196 propagation. The radius of curvature  $R_c$  of the EM-radiation propagating through a non-  
197 homogeneous region of material (also plasma) with permittivity  $\epsilon$  is given by  $R_c = \frac{2}{|\nabla(\ln \epsilon)|}$ ,  
198 which is along the principal normal vector  $\mathbf{n}$  of unity length [7]; the curvature is  $\kappa = 1/R_c$ . The  
199 gradient of refractive index will cause beam bending and consequently change of polarisation  
200 due to torsion along the propagation path, which can be accounted by the 3D vectorial analysis.  
201 The ray bending (a 3D curve) can be parametrised by the arc length  $s$  and the unit tangent vector  
202  $\mathbf{t}$ , which defines the bi-normal vector as  $\mathbf{b} = \mathbf{t} \times \mathbf{n}$  and forms the orthonormal set of unit vectors  
203  $[\mathbf{t}, \mathbf{n}, \mathbf{b}]$ , i.e., the Frenet–Serret frame. The  $E$ -field vector lies in the  $(bn)$ -plane. The torsion  $\tau(s)$   
204 measures the turnaround of the binormal vector along the arc  $s$  and cause rotation of the  $E$ -field  
205 (polarisation) by an angle  $\psi$ :  $\frac{d\psi}{ds} = 1/\sigma_t$  where  $\sigma_t$  is the radius of torsion [7]; torsion  $\tau = 1/\sigma_t$ .  
206 The curvature  $\kappa$  and torsion  $\tau$  (which are reciprocals to the radii of curvature  $R_c$  and torsion  $\sigma_t$ )  
207 enters derivatives along the curve  $s$  in the Frenet–Serret formulas:

$$\begin{bmatrix} d\mathbf{t}/ds \\ d\mathbf{n}/ds \\ d\mathbf{b}/ds \end{bmatrix} = \begin{bmatrix} 0 & \kappa & 0 \\ -\kappa & 0 & \tau \\ 0 & -\tau & 0 \end{bmatrix} \times \begin{bmatrix} \mathbf{t} \\ \mathbf{n} \\ \mathbf{b} \end{bmatrix}. \quad (\text{S6})$$

208 The formulae above can be used to establish characterisation method when well defined THz  
209 plane wave is probing the perturbed region, e.g., where shock wave is propagating.

## 210 References

- 211 1. C. D'Amico, A. Houard, M. Franco, B. Prade, , A. Mysyrowicz, A. Couairon, V. T. Tikhonchuk, *Phys. Phys. Lett.*  
212 **2007**, *98* 235002.  
213 2. B. H. Sang, T.-I. Jeon, *Opt. Express* **2016**, *24*, 25 279025.  
214 3. B. Campanella, S. Legnaioli, S. Pagnotta, F. Poggialini, V. Palleschi, *Atoms* **2019**, *7* 57.

- 215 4. S. Juodkazis, H. Misawa, E. G. Gamaly, B. Luther-Davis, L. Hallo, P. Nicolai, V. Tikhonchuk, J. Non-Crystall. Solids  
216 **2009**, 355, 18-21 1160.
- 217 5. E. Vanagas, J. Kawai, D. Tuzilin, I. Kudryashov, A. Mizuyama, K. G. Nakamura, K.-I. Kondo, S.-Y. Koshihara,  
218 M. Takesada, K. Matsuda, S. Juodkazis, V. Jarutis, S. Matsuo, H. Misawa, J. Microlith. Microfab. Microsyst. **2004**,  
219 3, 2 358.
- 220 6. E. E. Gamaly, S. Juodkazis, K. Nishimura, H. Misawa, B. Luther-Davies, L. Hallo, P. Nicolai, V. Tikhonchuk, Phys.  
221 Rev. B **2006**, 73 214101.
- 222 7. E. G. Gamaly, A. V. Rode, Appl. Phys. A **2018**, 124, 3 278.
- 223 8. L. D. Landau, E. M. Lifshitz, The Classical Theory of Fields - Course of Theoretical Physics, volume 2, Pergamon  
224 Press Ltd., Headington Hill Hall, Oxford, 3 edition, **1971**.
- 225 9. P. Gibbon, Short Pulse Laser Interactions with Matter: An Introduction, Imperial College Press, **2005**.
- 226 10. H. Schwoerer, South African J. Sci. **2008**, 104 299.
- 227 11. G. Mourou, T. Tajima, S. Bulanov, Rev. Modern Phys. **2006**, 78 309.